Applied Catalysis B: Environmental 331 (2023) 122597

Contents lists available at ScienceDirect

Applied Catalysis B: Environmental

journal homepage: www.elsevier.com/locate/apcatb

Hydrophobicity graded gas diffusion electrode with enhanced CO intermediate coverage for high-performance electroreduction of CO_2 to ethylene

Linbo Li [a,b], Xiaolong Zhang [c], Chuangwei Liu [d], Venkata Sai Sriram Mosali [a], Jun Chen [e], Alan M. Bond [a,b,*], Qinfen Gu [f,**], Jie Zhang [a,b,*]

[a] School of Chemistry, Monash University, Clayton 3800, Victoria, Australia
[b] ARC Centre of Excellence for Electromaterials Science, Monash University, Clayton 3800, Victoria, Australia
[c] Shenzhen Key Laboratory of Energy Materials for Carbon Neutrality, Shenzhen Institutes of Advanced Technology, Chinese Academy of Sciences, Shenzhen, 518055, China
[d] Key Lab for Anisotropy and Texture of Materials (MoE), School of Materials Science and Engineering, Northeastern University, Shenyang 110819, China
[e] ARC Centre of Excellence for Electromaterials Science, Intelligent Polymer Research Institute, Australian Institute for Innovative Materials, Innovation Campus, University of Wollongong, Squires Way, North Wollongong, NSW 2500, Australia
[f] Australian Synchrotron, ANSTO, Clayton 3168, Australia

ARTICLE INFO

Keywords:
Hydrophobicity graded gas diffusion layer
Electrochemical CO_2 reduction
Stable ethylene production
Enhanced CO intermediate coverage
Polytetrafluoroethylene

ABSTRACT

Electroreduction using a gas diffusion electrode (GDE) provides an efficient method for high rate conversion of CO_2 to value-added chemicals. However, long term production with high yields remains challenging due to rapid electrolyte flooding through the hydrophobic gas diffusion layer (GDL). Here, we report a universal strategy to convert a commercial GDL into a hydrophobicity graded GDL (HGGDL) that resists electrolyte flooding. The CO_2 electroreduction performance of a family of tandem catalysts consisting of a nickel-single-atom catalyst and Cu nanoparticles immobilized on GDLs and HGGDLs is compared with respect to ethylene production. *In situ* Raman studies reveal that the HGGDL increases the CO intermediate coverage as a result of the higher differential pressure across the electrodes. Lower carbonate formation also is observed. Enhanced ethylene production efficiency and an order of magnitude improvement in long term stability is achieved in a membrane electrode assembly electrolyzer.

1. Introduction

The electrochemical CO_2 reduction reaction (ECO_2RR) offers a green and potentially economic route that mitigates environmental impacts of the greenhouse gas CO_2 while storing renewable energy as value-added chemicals [1–4]. Multicarbon (C_{2+}) products, such as ethylene, which are of particular interest in this study, are more profitable than single carbon (C_1) products because of their higher commercial values and energy density [1,5,6]. Since reduction of CO_2 is kinetically slow, catalysts are needed to overcome the high activation barrier and enhance the kinetics. Of the catalysts reported so far, copper (Cu) is the only metal that can produce ethylene at an appreciable rate but only at a high overpotential and with poor product selectivity [2,3,7]. In recent years, nano-engineering strategies such as morphological, facet and defect control [8,9], alloying [10,11], and molecular modification [12,13], have substantially improved the performance of Cu-based catalysts for C_2H_4 production. Using a gas diffusion electrode (GDE) to minimise the CO_2 mass transfer limitation, state-of-the-art CO_2 electrolysers now have industrially relevant capabilities; specifically, C_2H_4 partial current density (j_{C2H4}) > 100 mA cm^{-2} and faradaic efficiency (FE_{C2H4}) > 60% [9,13].

Despite a series of breakthroughs, development of a commercially viable process for electrosynthesis of C_2H_4 from CO_2 with high selectivity, activity, and stability remains challenging [13,14]. One of the major technical challenges is the instability of the GDE due to electrolyte flooding in the hydrophobic carbon gas diffusion layer (GDL), a major component of the GDE [15,16]. The GDL typically comprises a hydrophobic bilayer structure including a carbon fiber macro-porous backing

* Corresponding authors at: School of Chemistry, Monash University, Clayton 3800, Victoria, Australia
** Corresponding author.
E-mail addresses: Alan.Bond@monash.edu (A.M. Bond), qinfeng@ansto.gov.au (Q. Gu), jie.zhang@monash.edu (J. Zhang).

https://doi.org/10.1016/j.apcatb.2023.122597
Received 3 October 2022; Received in revised form 11 January 2023; Accepted 6 March 2023
Available online 10 March 2023
0926-3373/© 2023 The Author(s). Published by Elsevier B.V. This is an open access article under the CC BY-NC-ND license (http://creativecommons.org/licenses/by-nc-nd/4.0/).

support (MBS) and a micro-porous layer (MPL) (Fig. 1a). Hydrophobicity of MPL and MBS is crucial for maintaining the electrode surface tension of GDL, thereby ensuring the local pressure between gas-liquid interfaces is sufficient to prevent electrolyte intrusion and also to sustain high mass transport rates of CO_2 and gaseous products in the GDL [17,18]. Despite improvements in carbon GDL, the commercial carbon GDLs still suffer from electrolyte flooding and gas blocking, after a few hours of operation under CO_2 electrolysis condition [19–22].

The highly alkaline local environment formed during CO_2 electrolysis favours C_2H_4 selectivity by the inhibition of the hydrogen evolution reaction (HER) [23,24]. However, it also results in the carbonation of the electrolyte which leads to salt precipitation [21,25]. As the generated carbonate is hygroscopic, the precipitated salts impair the hydrophobicity of the GDL and hence destabilize the CO_2–catalyst–electrolyte three-phase interface for the ECO_2RR [20,26]. This implies that solutions to this problem may lie in the rational design of the GDL structures that minimise the degradation of the delicate three-phase interfaces present in a porous GDL [15,26–28].

Recently, we have reported a simple and easily scalable method for the fabrication of a hydrophobicity graded GDL (HGGDL) from a hydrophilic one [22]. The reported HGGDL not only mitigates electrolyte flooding of the GDL but also can be applied to catalysts that cannot be sputtered or have low electrical conductivity. In current work, we investigate the influence of sintering on pore size as well as contract angle of the resulting HGGDL. Here, we present a method for coating the MPL of a commercial hydrophobic GDL with a polytetrafluoroethylene (PTFE) macroporous layer (PMPL) to develop a HGGDL. The general applicability of this method is demonstrated using three of the most popular GDLs (See **Materials** and **Methods**). The hydrophobicity-graded strategy enhances the hydrophobicity of the GDL, controls the pore size and narrows the pore size distribution, and hence increases the local pressure across the GDL and provides stability against electrolyte flooding. We further examine the effect of the HGGDL on stable electrochemical reduction of CO_2 to C_2H_4 that is catalyzed by tandem catalysts consisting of nickel single-atom-N-doped graphitic carbon (NiNG) and Cu nanoparticles (CuNPs) [29–32]. *In situ* Raman spectroscopic studies show that the HGGDL not only enhances the CO surface coverage but also decreases the CO_2 concentration adjacent to the Cu sites. The lower CO_2 concentrations and hence lower carbonate production on the HGGDL-based electrode (HGGDE), improve the stability of gas-solid-liquid three-phase interfaces present in the electrode. As a result, a FE_{C2H4} of 61% ± 5% at − 0.58 V versus the reversible hydrogen electrode (RHE), a full-cell energy efficiency of 17% and an order of magnitude improvement in C_2H_4 production stability have been achieved in a membrane electrode assembly electrolyzer.

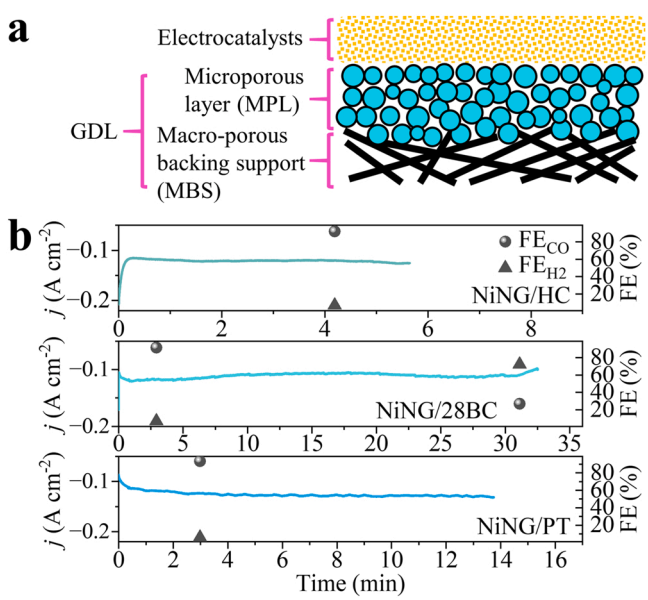

Fig. 1. Commercial GDLs and their performance. a, A schematic illustration of the major components of a typical commercial carbon GDL. b, Chronoamperometric data recorded during CO_2 electrolysis in 1 M KOH in a flow cell using 28BC, HC, and PT GDLs coated with the NiNG catalyst.

2. Experimental section

2.1. Materials

60 wt% PTFE emulsion (POLYFLON PTFE D-210 C, Daikin, nonionic surfactant: polyoxyethene glycol alkyl ether < 5%), P75T (PT, AvCarb), H14C9 (HC, Freudenberg), Sigracet 28BC (28BC, SGL Carbon), sodium hypophosphite hydrate ($NaH_2PO_2{\cdot}H_2O$, 99%, Sigma), nickel nitrate hexahydrate ($NiNO_3{\bullet}6\ H_2O$, 99%, Sigma), polyvinyl pyrrolidone (PVP, average Mw: 40000, Sigma), natural graphite powder (size < 45 μm, 99.99%, Sigma), *n*-hexane anhydrous (95%, Sigma), airbrush (H-Set single action, Paasche), anion-exchange membranes (Fumapem FAA-3-PK-130 for liquid-electrolyte flow cell, Sustainion X37–50 grade 60 for membrane electrode assembly electrolyzer), dimethylsulfoxide (DMSO, ≥ 99.9%, Alfa Aesar), deuteroxide (D_2O, 99.9%, Sigma), high purity (99.99%, BOC Gas) CO_2, H_2, Helium, Ar. All aqueous solutions were prepared using deionized (DI) water (Milli-Q, resistivity 18 MΩ • cm).

2.2. Methods

2.2.1. Preparation of HGGDL by the hydrophobicity graded process

A piece of commercial 28BC, taken as an example, was firstly placed on a dry polyurethane-based acoustic sponge with the graphite flake-based MPL side that is in contact with the CO_2 gas during electrolysis facing upward. Before hydrophobicity-graded treatments, two edges of graphite flake-based MPL of 28BC were covered with conductive copper tapes to protect the two edges from covering by PTFE nanorods. This procedure ensures the good electrical conductivity of PTFE coated graphite flake-based side of the final HG28BC GDL for the membrane electrode assembly electrolyser. A blade brush with soft nylon bristles or an airbrush was only used to paint the graphite flake-based MPL surface with an X wt% (X = 30, 40, 50, 55 and 60) of PTFE emulsion (step 1: PTFE coating, Fig. S1 and Fig. 2). The painting process was performed to ensure a uniform dispersion of PTFE emulsion on the graphite flake-based MPL surface. The carbon-nanoparticle based MPL served as both catalyst support and current collector, and was not treated with PTFE emulsion. Thus, the amount of PTFE modification will not affect the conductivity of the electrodes [22]. After drying in air for around 2 min, the PTFE-coated 28BC was transferred onto a dry acoustic sponge. To avoid residual PTFE emulsion blocking the MPL channels of 28BC, an airbrush connected with a N_2 valve (0.5 bar) was used to blow the whole MPL surface using a 5 mm gap between the airbrush tip and the MPL surface (step 2: Airbrush blowing, Fig. 2). In this step, the acoustic sponge was used to support the whole GDL (carbon-nanoparticle based MPL side facing upward), while allowing N_2 gas to flow though at high speed. Next, the PTFE-coated 28BC was washed with hexane in a beaker (step 3: Hexane cleaning, Fig. 2), then again transferred to a sponge and dried with an air brush following the procedure described in step 2 (step 4: airbrush blowing, Fig. 2). After repeating steps 3 and 4 once or twice, we replaced the conductive Cu tapes (that might be covered by PTFE nanorods) with new conductive Cu tapes on the edges of the GDL, which was then transferred to a quartz boat and placed in a tube furnace for sintering under a N_2 atmosphere (step 5: sintering, Fig. 2). The steps involved are schematically summarized in Fig. 2a. The temperature program used for sintering was: (1) heating to 200 °C from room temperature using a ramping rate of 5 °C min^{-1}; (2) maintaining the temperature at 200 °C for 10 min; (3) heating to higher temperature (250, 300, 320, 330, 340, 350, or 360) using a 1 °C min^{-1} ramping rate; (4) maintaining at the highest temperature for 1 h and (5) cooling down

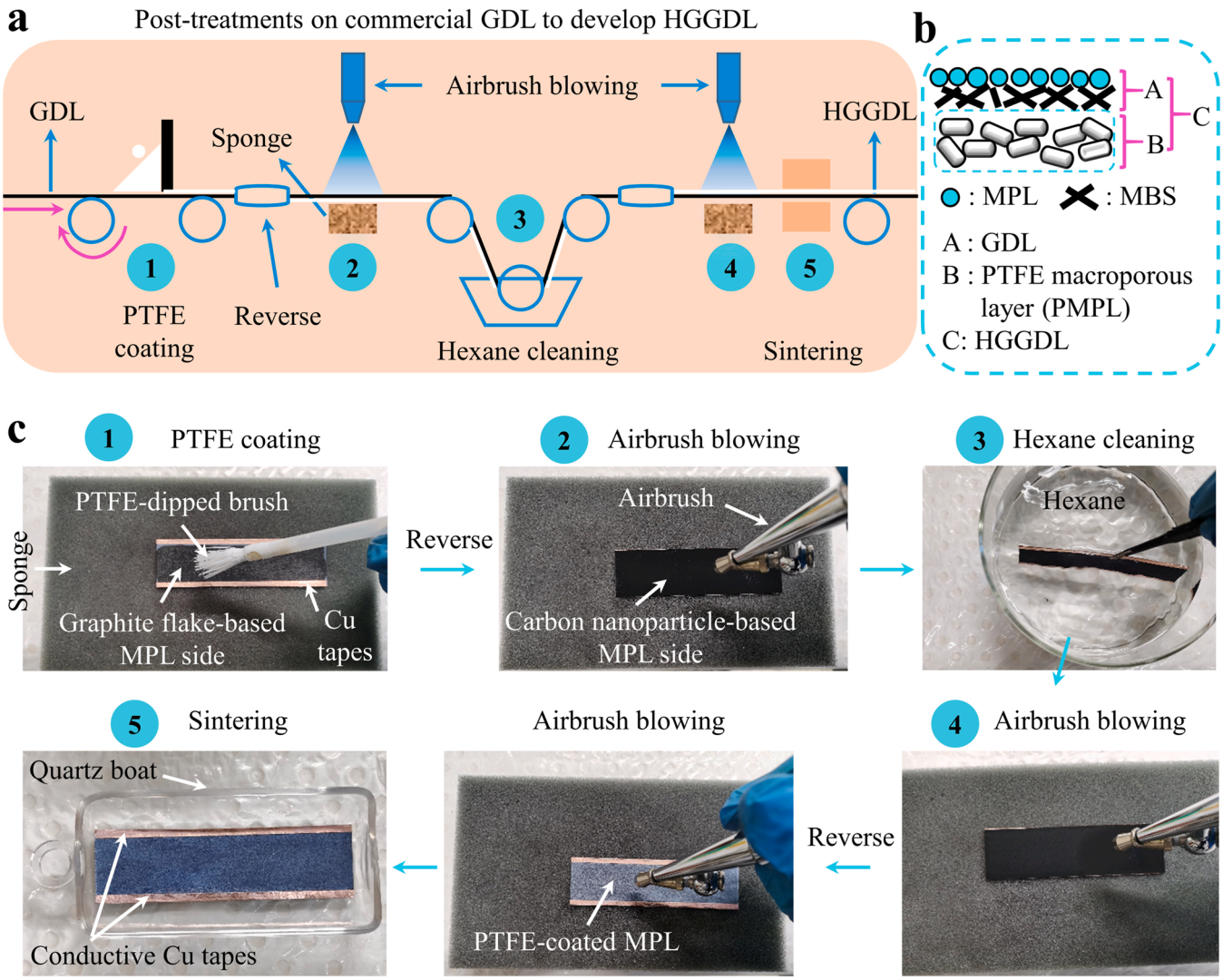

Fig. 2. Fabrication of a HGGDL. a, Schematic diagram. b, Schematic illustration of the major components of the HGGDL. **c**, Demonstration with 28BC, of which two graphite-based MPL edges were covered with conductive copper tapes.

naturally to room temperature. 28BC treated by this process is denoted as HG28BC. Similar procedures were also applied to prepare hydrophobicity-graded 28BC (CB-HG28BC) as a control by using the carbon nanoparticle-based MPL as the side for PTFE coating (Fig. S26). The same process was also used to treat two other types of GDLs: HC and PT, to give as HGHC and HGPT, respectively.

2.2.2. Synthesis of Cu nanoparticles

Cu nanoparticles were prepared by modifying a published procedure [33]. 0.02 mol $NaH_2PO_2{\cdot}H_2O$ and 2 g PVP were added to 40 mL ethylene glycol under vigorous stirring. The mixture was then heated to 90 °C to form solution A. 0.01 mol $CuSO_4$ was dissolved in 10 mL ethylene glycol and then heated to 90 °C to form solution B which was rapidly injected into solution A under vigorous stirring. The color of the solution rapidly changed from green to dark red brown as a result of CuNP formation. The reaction was rapidly quenched by adding chilled water. The CuNPs were separated by centrifugation, re-dispersed in acetone and separated again by centrifugation. This process was repeated three times. The final CuNP powder was dried and stored under vacuum at room temperature prior to application. All procedures were carried out under a N_2 atmosphere to minimize oxidation of CuNPs.

2.2.3. Fabrication of membrane electrode assembly

The MEA setup is a 1.5 * 2 cm^2 gas electrolyzer having both a titanium anode and cathode plate. A single serpentine flow-field having a 0.9 mm channel depth, a 0.9 mm channel width, and a 0.9 mm rib width was machined on one side of each plate. The anode (IrOx/Ti mesh) was constructed using a modified dip coating and thermal decomposition method [34]. Specifically, Ti mesh was etched in boiling oxalic acid (0.5 M) for 1 h. The mesh then was rinsed with $IrCl_3{\cdot}xH_2O$ (3 mg mL^{-1}) dissolved 2-propanol solution (containing 20% volume concentrated HCl) droplets followed by drying under an IR lamp. After repeating this step several times, the mesh was calcined in air using the program: room temperature to 500 °C with a 5 °C min^{-1} ramping rate; maintained at 500 °C for 20 min. The procedure was repeated twice to form the IrOx/Ti mesh anode. The catalyst deposited HG28BC cathode, coated with PMPL on the graphite-based MPL, was mounted on a flat titanium plate without a flow field. Sustainion X37–50 grade 60 (Dioxide Materials, USA) with high ion-conductivity was used as the anion exchange membrane (AEM) to sandwich the anode and cathode. The edges of the AEM were partially covered by parafilm to protect the cathode from contact with electrolyte. Subsequently, another flat titanium plate was placed on the anode and then bolted to compact the MEA. The prepared MEA was transferred and fixed to the cathode Ti plate and then covered with anode Ti plate. Finally, we bolted the MEA setup.

2.2.4. Synthesis of NiNG and NG

These catalysts were derived from a reported method [22]. 0.2 g of graphite powder was mixed with water (90 mL) in a conical flask under intensive sonication for 30 min to form suspension A. Aqueous ammonia solution (30 wt%, 2 mL) and ethanol (99.9%, 40 mL) were successively added into suspension A while stirring. Subsequently, a 10 mL aqueous solution containing dopamine hydrochloride (0.5 g) and $NiNO_3$•6 H_2O (10 mg) was added dropwise. The flask was then sealed and the mixture stirred overnight under ambient conditions. A precipitate was obtained by centrifugation at 18000 rpm, re-dispersed in acetone and again separated by centrifugation at 18000 rpm. This process was repeated 3 times. The final product was dried under a N_2 atmosphere at 60 °C for 24 h. The dry precipitate was mixed uniformly with dicyandiamide in a weight ratio of 1:10 by grinding. The ground powder then was loaded into a quartz boat and transferred into a temperature-programmed furnace for pyrolysis under an Ar flow. The temperature program for pyrolysis was: (1) heating to 800 °C from room temperature using a 5 °C min^{-1} ramping rate; (2) sustaining at 800 °C for 2 h; (3) cooling down naturally to room temperature. The as synthesized Ni-N doped carbon materials were soaked in 20 mL of 1 M H_2SO_4 overnight. The resultant NiNG was collected after centrifugation, washed with water and acetone (at last twice) and dried under vacuum at room temperature.

NG was prepared as described above except that no $NiNO_3$•6 H_2O was added.

2.2.5. Preparation of working electrodes

2.8 mg of catalyst (CuNPs, NiNG or their mixtures with designated ratios) and 5 μL Nafion (5 wt%) were added into 1.0 mL of 2-propanol. The suspension was sonicated for 20 min to achieve a homogeneous ink. A known volume of the ink was drop-cast onto the GDL and then dried under an N_2-atomosphere to obtain a working electrode. As for the CuNPs/28 wt% NiNG catalyst, the Ni loading at the cathode is ~0.2 mg cm^{-2}.

2.3. Characterization

Scanning electron microscopy (SEM, FEI Quanta 3D FEG, FEI Nova NanoSEM 450 FEG, FEI Magellan 400 FEG and Thermo Scientific Phenom Pharos PW-100–160), transmission electron microscopy (TEM, FEI Tecnai G2 T20 TWIN and FEI Tecnai G2 F20 S-TWIN) and probe corrected scanning transmission electron microscope (STEM, JEOL JEM-ARM200F) were employed to image samples. Prior to imaging, all the GDLs modified with PTFE macroporous layer (PMPL) were coated with a thin layer of gold or palladium particles using a Gatan 682 precision etching and coating system.

X-Ray Diffraction (XRD) measurements were undertaken with a Bruker D8 ADVANCE X-ray powder diffractometer (Cu Kα radiation, $\lambda = 0.15406$ nm). X-ray photoelectron spectroscopy (XPS) was performed with a Thermo Scientific Nexsa Surface Analysis System equipped with a hemispherical analyser. The incident radiation was monochromatic Al Kα X-rays (1486.6 eV) at 72 W (6 mA and 12 kV, 400 × 800 μm^2 oval spot). All XPS data were charge-calibrated using adventitious carbon (284.8 eV). Dynamic light scattering analyses were performed with a Mastersizer 2000 (Malvern Instruments) at 25 °C (three replicates).

Mercury intrusion porosimetry (MIP) analyses were conducted to evaluate the porosity, pore size distribution and pore volume of the GDLs using a Micrometrics Instrument Corporation (USA) AutoPore IV 9500 apparatus with ≥ 0.05 g of GDL samples (1.2 *1.2 cm^2/piece) and a 3.37 mL volume penetrometer.

The contact angles (CA) of water (10 μL) were measured using an OCA 20 instrument (Dataphysics, Germany). The CA values are recorded as the average of three measurements obtained from different positions.

In situ Raman measurements were obtained in a home-made flow cell using a Renishaw inVia Raman microscope and a water immersion objective (Germany, Leica, 40X / 0.80) with a 633 nm laser, employing a binning value of 3–4, 3 accumulations, 10 s exposure time, 5–10% laser power and averaging 10 scans per region. During measurements, CO_2 was continuously flowed through the flow cell at a rate of 20 standard cubic centimeters per minute (SCCM). The quasi-operando XAS (X-ray absorption spectroscopy) measurements were undertaken after electrolysis at designated potentials using the X-ray absorption spectroscopy beamline in the fluorescence mode at the Australian Synchrotron (ANSTO). ^{1}H NMR experiments were undertaken with a Bruker 600 MHz NMR spectrometer using a 5 mm broadband autotunable probe with Z-gradients.

2.4. Electrochemical CO_2 reduction and product analysis

The electrochemical tests were conducted in a liquid-electrolyte flow cell setup at 25 °C. An anion exchange membrane (Fumasep FAB-PK-130) was used to separate the cathode and nickel foam/plate (geometric area ~1.5 cm^2) anode. 1 M KOH electrolyte was pumped into both the cathodic and anodic chambers of the flow cell at a flow rate of 5–10 mL min^{-1} using a peristaltic pump (Thermonline BT100–2 J+DG-4A) with 2 (inner diameter) × 1 (tube thickness) mm tubing (Ditrontech). The 10–20 sccm high purity CO_2 gas was introduced to the cathodic gas chamber by a mass flow controller (Cole-Parmer 32907–63). A VoltaLab40 PGZ301 electrochemical workstation under potentiostatic control was employed in electrochemical measurements using an HGGDL based working electrode with or without catalyst, an Hg/HgO (1 M KOH, BASi) reference electrode and a nickel foam/plate (0.1 mm thickness) counter electrode. All potentials (unless specifically specified) were converted to the reversible hydrogen electrode (RHE) scale with inclusion iR_u drop (η_{IRu}, R_u: uncompensated resistance of electrolyte solution, i: cell current) using: E (vs. RHE) = E (vs. Hg/HgO) + 0.14 V + 0.0591 V × pH + η_{IRu}. The value of R_u was determined by electrochemical impedance spectroscopy (EIS) at the open circuit potential (OCP) using an amplitude of 5 mV and at frequency range of 10^{-2} to 10^5 Hz. The cell current was averaged for at least 10 min at the applied potential. The pH data for the electrolyte effluents were measured with a SevenCompact pH/Ion meter S220 (Mettler Toledo, USA). The stability measurements in the liquid flow-cell were undertaken in 1 M KOH at − 0.53 V with a flow rate of 20 SCCM using GDEs loaded with 0.18 mg cm^{-2} of catalyst.

The ECO_2RR gas products were determined using an online gas chromatograph (SRI 8610 C, MG #5) equipped with a thermal conductivity detector (TCD) and a flame ionization detector (FID). Using the temperature program (from 70 °C to 250 °C), it took the GC 21.25 min to separate and detect gas products and ~2 min to cool the column to 70 °C. Consequently, each GC measurement has an interval of ~ 23 min. The carrier gas was helium. For each applied potential, 1 mL of the effluent gas flow was periodically sampled and transferred into a gas chromatograph. A soap-film flowmeter (100 mL) was used to monitor the flow rate of effluent gas to ensure the accuracy of gas flow rate (Fig. S2). The FEs for gases was determined using the formula:

$$FE(\%) = \frac{zFn\vartheta}{IV} * 100\% \quad \text{(E1)}$$

where z is the number of electrons transferred, F is Faraday's constant, n is the moles of product, ϑ is the flow rate (mL min^{-1}) of gas, V is the injected volume (mL) of mixed gas and I (mA) is the total current at the time of commencing sampling. Liquid products were analyzed by a Bruker 600 MHz NMR spectrometer using water suppression with a presaturation method. Specifically, 0.50 mL of the catholyte was mixed with 0.10 mL of D_2O and 100 ppm (v/v) DMSO added to provide an internal standard.

The single pass carbon utilization (SPU) of CO_2 towards ethylene was calculated using the following equation at 25 °C, 1 atm [35]:

$$\mathrm{SPU} = \frac{j}{NF\vartheta} \tag{E2}$$

where j is the partial current of ethylene from CO_2 reduction, N is the number of electrons transferred for every ethylene molecule. F is Faraday's constant and ϑ is the flow rate (mL min^{-1}) of CO_2.

3. Results and discussion

3.1. Preparation of a Hydrophobicity Graded GDL

Experiments were first undertaken to investigate the stability of three commercial wet-proofed GDLs (28BC, PT, and HC) against electrolyte flooding during CO_2 electrolysis in a flow cell with a nickel single-atom-N-doped graphitic carbon (NiNG) catalyst, in which the Ni

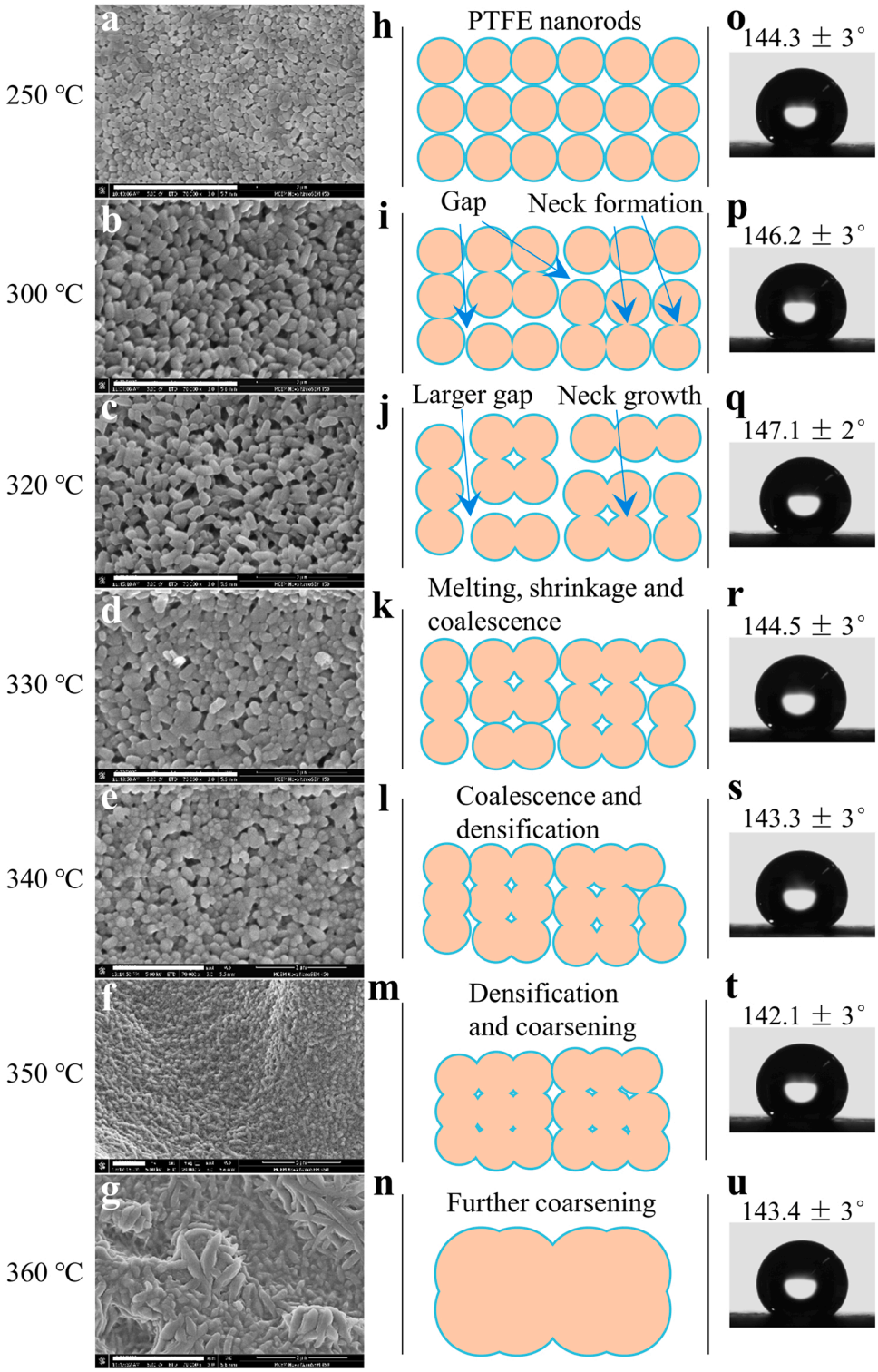

Fig. 3. Characterization of the PMPL of HG28BC GDLs sintered at the designated temperatures. Front-view SEM images (a-g), schematic illustration of sintering PTFE nanorods (h-n) and contact angles (o-u). The scale bar of SEM images: 2 μm. Prior to sintering, the PTFE loading of all GDLs is ~4.5 mg cm^{-2}.

atoms are preferentially coordinated with pyridinic N (Fig. S3 - Fig. S5 **Supplementary Note 1**). XRD spectra, SEM images and specifications of these GDLs are given in Fig. S6 Fig. S9 and Table S1. The GDL structure is schematically illustrated in Fig. 1a and the current density (*j*) versus time (t) data recorded in a chronoamperometric experiment for each GDL are shown in Fig. 1b. Despite being functionalized with carbon-based MPL and having a high loading of PTFE, all three commercial GDLs suffered from electrolyte flooding (see V1-V6 in video attachments) even though some of them may still show stable current densities for 1 h during CO_2 electrolysis in the presence (Fig. 1b) or absence (Fig. S10a) of the NiNG catalyst. Furthermore, an increasing FE_{H2}/FE_{CO} ratio was found for the NiNG/28BC electrode, which also confirmed the occurrence of electrolyte flooding on the NiNG/28BC electrode (Fig. 1b).

To overcome drawbacks associated with the commercial GDLs, we have developed a simple and easily scalable method to control the pore size distribution and grade the hydrophobicity of the GDLs but without affecting their electrical contact with the catalyst. In this method, the commercial hydrophobic GDL is treated by a procedure involving a series of steps: PTFE coating, airbrush blowing, hexane cleaning, airbrush blowing and sintering to prepare a hydrophobicity graded GDL (HGGDL) using a PTFE macroporous layer (PMPL) coated on one side of the GDL (Fig. 2a,b). This method is shown schematically in Fig. 2b and demonstrated using a 28BC GDL as an example in Fig. 2c.

A nonpolar solvent, such as hexane, instead of a polar solvent, such as water or ethanol, was used to clean PTFE coated 28BC (**Fig. 2**c3). This avoids re-dispersion (occurred when treated with water, Fig. S11b) and flocculation (occurred when treated with ethanol, Fig. S11c) of PTFE nanorods, resulting in a uniform PTFE coating (Fig. S12). Note that hexane cleaning also favors the removal of nonionic surfactant from PTFE-coated 28BC, exposing more bare PTFE nanorods and thus increasing the hydrophobicity of the treated 28BC [22]. Further details related to HGGDL fabrication are given in the **Methods** section.

The final sintering step, which was performed near the melting point of PTFE (327 °C), is crucial to control the pore size and to ensure strong adhesion of the PMPL with the GDL (**Fig. 2**c5, Fig. 3 a–n, Fig. S13). The effect of the sintering temperatures on the structural properties of HG28BC was explored. Front-view and cross-section SEM images showed that the morphology of the PMPL with sintered HG28BC GDLs gradually changed from closely stacked at 250 °C to a compact porous network, especially at 320 °C. Subsequently, the porous network shrank and coalesced into a highly densified and coarsened PTFE film at 360 °C (Fig. 3 a-g, Fig. S14-S16). This PMPL morphology evolution can be schematically summarized by use of models which depict three stages of PMPL restructuring driven by sintering (Fig. 3 h-n). Note that the models used in Fig. 3h-n only consider the interactions between PTFE nanorods but do not consider the formation of macropores and cracks of PMPL during the hydrophobicity-graded process (Fig. S17).

During sintering, slow decomposition of PTFE occurs from 260 °C and becomes more significant when the temperature increases [36]. The surface loss of PTFE nanorods speeds up with the increase of sintering temperature, which is accompanied by variation in pore/gap size [37]. Initially, a neck is formed between the PTFE nanorods via mass transport, which grows rapidly as the temperature is increased from 250 °C to 320 °C. An apparent evolution of the pore morphology could be observed (Fig. 3a-c, Fig. S14a-c and Fig. S16a-c). During this stage, the free surface area and porosity of PMPL remain high. This indicates that surface diffusion drives the material from the PTFE nanorods to the neck surface since no obvious shrinkage of PTFE nanorods was observed (Fig. 3 h-j) [38,39]. As the melting point of PTFE is 327 °C, PTFE nanorods start to melt over 330 °C. Shrinkage and coalescence of PTFE nanorods on a macroscopic level was then found by a progressive decrease of the distance between the centers of PTFE nanorods (Fig. 3k). In the temperature range from 330 °C to 340 °C, surface curvature is further reduced with neck growth, leading to a densified and coalescent PMPL (Fig. 3 k and l). At temperatures higher than 350 °C, the final sintering stage is accompanied by complete removal of porosity of the coarsening PMPL, which minimizes the overall interfacial free energy (Fig. 3 m and n) [40,41].

The increase in the sintering temperature has negligible effect on the size distribution of the small pores but decreases the size distribution of the large ones (Fig. S13a and Table S2). The porosity follows a volcano trend peaking at 320 °C when the sintering temperature is increased from 250° to 360°C, while the hydrophobicity of the PMPL on HG28BC GDLs remains unaltered based on the contact angle data (Fig. 3 o-u; Fig. S13b, Table S2). The observed trend in porosity might be attributed to the evaporation/decomposition of some components during sintering at 250 °C and/or rearrangement of PTFE nanorods as mentioned for PTFE sintering in Fig. 3a-n [37]. In combination with the SEM images (Fig. S7 - Fig. S9; Fig. 3, a-g; Fig. S24; Fig. S25), the MIP–pore size distribution data for HG28BC, HGPT, and HGHC confirm that the average sizes of large pores are significantly diminished in comparison with their unmodified counterparts (Fig. S13a and Fig. S18 c and d). Thus, the sintering step can efficiently narrow the pore size distribution of the GDL. According to the Young-Laplace equation, a sufficient capillary pressure difference between the catholyte and CO_2 gas phases under flow cell conditions is inversely proportional to the pore radius of a hydrophobic pore [42]. This implies that electrolyte flooding tends to occur preferentially through the large pores or cracks [43]. Thus, the ability to control the pore size distribution of a GDL is desirable to mitigate electrolyte flooding. On the basis of cost and pore size distribution, 320 °C was selected as the sintering temperature in subsequent applications.

The influence of the concentration of the PTFE emulsion used for PTFE coating, on PTFE loading, conductivity and the stability of the HGGDLs against electrolyte flooding was investigated in more detail. The results suggest that the PTFE loading, determined on the basis of the mass difference per cm^2 before and after PTFE coating on the HG28BC GDLs, increased linearly with the concentration of the PTFE emulsion (Fig. S19). Similar features in linear sweep voltammograms were obtained using bare 28BC and HG28BC based GDLs, indicating that PTFE loading has no significant effect on the electric conductivity of the HGGDL (Fig. S20). The anti-flooding properties of all modified HGGDLs (HG28BC, HGPT, HGHC) were assessed using NiNG as the catalyst and 1 M KOH as the electrolyte (Fig. 4 and Fig. S21). The optimal PTFE loading for the HG28BC, based on CO_2 electrolysis durability, is ~4.5 mg cm^{-2} using the PTFE emulsion (~55 wt%) for the coating. In this case, the stability duration of NiNG/HG28BC electrode was > 12 h, which is more than 24 times that found with an unmodified 28BC-based counterpart (0.5 h) (Fig. 1b, Fig. 4, Table S1). The durability

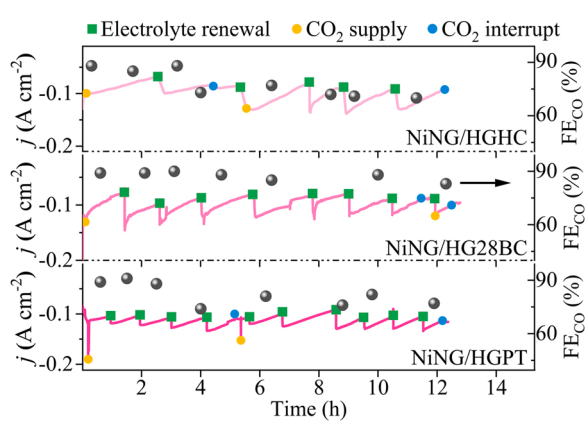

Fig. 4. Performance of a hydrophobicity graded GDL in a flow cell. Chronoamperometric data recorded in 1 M KOH in a flow cell using hydrophobicity-graded 28BC, HC, and PT GDLs coated with the NiNG catalyst. Note: Green square: time at which fresh electrolyte was pumped into the catholyte chamber; Blue dot: time when the CO_2 gas flow was stopped; Yellow dot: time when the CO_2 gas flow was restored.

improvements for HGPT and HGHC GDLs treated using the PTFE emulsion (~55 wt%) were > 51 and > 120 times, respectively (Fig. 1b, Fig. 4, Table S1). Fig. 4 shows the current decay that occurs during electrolysis due to local carbonation of the electrolyte which consumed some of the CO_2 feed [15,20]. Significantly, after renewal with a fresh electrolyte, the current magnitude was recovered. After electrolysis, the PMPL sides of all electrodes (NiNG/HG28BC, NiNG/HGPT, NiNG/HGHC) retained their porous compact PTFE-nanorod networks and hydrophobicity (Fig. S22 - Fig. S25). These findings confirm the durability of the electrodes.

Fig. 4 also shows that the average FE_{CO} on NiNG/HGHC, NiNG/HG28BC, NiNG/HGPT electrode is 78 ± 8%, 87 ± 3%, 82 ± 7%, respectively. Note that the relative standard deviation of FE_{CO} for NiNG/HG28BC electrode is much lower than the other two electrodes. This indicates that the fluctuation of FE_{CO} for NiNG/HG28BC electrode is significantly less than the other two electrodes. Contrary to HGPT and HGHC GDLs, the fraction of small pores (size ranging from 0.03 μm to 2 μm) in HG28BC dominates the pore size distribution because the portion of large pores has significantly decreased (Fig. S7 - Fig. S9, Fig. S13, Table S2). The narrower pore size distribution of HG28BC GDL favours a more uniform CO_2 gas distribution across the GDL. This presumably accounts for the finding that the HG28BC based electrode achieved a more stable CO production compared with the NiNG/HGPT and NiNG/HGHC electrodes (Fig. 4). We further carried out similar procedures to prepare hydrophobicity-graded 28BC (CB-HG28BC) as control by using the carbon nanoparticle-based MPL side for PTFE coating (Fig. S26a and b). Fig. S26c shows that the carbon nanoparticle-based MPL is covered by a flat and compact PMPL. In contrast with that found on the graphite flake-based MPL of HG28BC (Fig. S12b and f, S17, S22 and S23), no macropores are present in CB-HG28BC. This accounts for that the fraction of larger pores ranging from 0.2 μm to 10 μm in CB-HG28BC was considerably lower than raw 28BC and HG28 BCE (Fig. S26d). Accordingly, the chronoamperometric data recorded using CB-HG28 BCE coated with NiNG catalysts shows a significant current fluctuation due to gas blocking, which is supported by the obvious fluctuation in FECO during electrolysis (Fig. S26e). Hence, it is worth further investigating the ECO_2RR performance of the HG28 BCE GDL with medium porosity, pore size distribution and hydrophobicity. Using NiNG/HG28 BCE electrode, chronopotentiometric data collected at a constant current density of 100 mA cm^{-2} shows a result consistent with the chronoamperometric data presented in Fig. 4 (Fig. S27).

3.2. ECO_2RR performance

Initially, the electrochemical performances of NiNG catalysts for ECO_2RR to CO was investigated. Without incorporation of Ni single atoms into carbon supports, the graphite and NG produced mostly H_2 with a small amount of formate (Fig. S28). In contrast, CO FEs for NiNG had a maximum value of (94.5%) at ~ − 0.6 V, with values exceeding 50% over a wide potential range from − 0.2 V to − 0.8 V (Fig. 5a). This provides an adequate CO supply to Cu sites for tuning the C-C coupling pathways [44].

Subsequently, Cu nanoparticles (CuNPs) were prepared by a solvothermal reduction method [33]. The CuNPs prepared are Cu(111) facet dominant polycrystalline materials with an average size of 68 ± 2 nm and a major valence of zero (Fig. S29).

CuNPs were incorporated into the NiNG catalyst to form a family of CuNPs/NiNG tandem catalysts to probe the ECO_2RR performance on the HG28 BCE-based electrode (Fig. 5). Five types of CuNPs/NiNG tandem catalysts were prepared [29,44,45]. Ethylene production with all the catalysts deposited on a HG28 BCE GDL was measured with the same loading in an aqueous flow cell. Results show that the C_2H_4 selectivity obtained with all the CuNPs/NiNG tandem catalysts was significantly better than obtained with pure CuNPs (Fig. 5b). The mixture containing NiNG (28 wt%) and CuNPs (CuNPs/28 wt% NiNG) achieved the best C_2H_4 FE of 61.1%, which is 1.5 times that of CuNPs (C_2H_4 FE 41.2%) (Fig. 5b and Fig. S30).

The ECO_2RR performance of the CuNPs/28 wt% NiNG and CuNPs deposited onto the HG28 BCE GDL and 28 BCE GDL also was studied over a wide potential range. To establish the product distribution, potentiostatic electrolyses were conducted over the potential range of − 0.25 to − 0.79 V vs RHE (Fig. S31). The FE for each product obtained with the CuNPs/28 wt% NiNG/HG28 BCE electrode is shown in Fig. S31 as a function of potential. A FE_{C2H4} of 2.1% with CuNPs/28 wt% NiNG/HG28 BCE electrode was found at − 0.28 V vs RHE which initially increased when the applied potential was made more negative, reaching a maximum value of 61.1% at − 0.58 V vs RHE, before decreasing at more negative potentials. As expected, a similar product distribution was found when CuNPs/28 wt% NiNG was deposited on raw 28 BCE (Fig. S31), since the product distribution is mainly governed by the catalyst. In contrast, the C_2H_4 formation onset potential was more negative, and C_2H_4 selectivity was significantly worse when CuNPs alone were deposited on either modified or unmodified 28 BCE GDLs (Fig. S31, b and d). Specifically, at − 0.63 V, the highest FE for C_2H_4 of only 41.2%, was obtained on CuNPs (Fig. S31). The j_{C2H4} values as a function of applied potential are shown in Fig. 5c. At − 0.67 V where j_{C2H4} with CuNPs/28 wt% NiNG was the highest, the j_{C2H4} obtained with the CuNPs/28 wt% NiNG is ~230 mA cm^{-2}, which is ~1.3 times that of the maximum value for CuNPs obtained at − 0.63 V (175 mA cm^{-2}). This results concur with literature findings that enhanced C_2H_4 selectivity and activity is achieved with tandem catalysts [13,46].

3.3. Mechanistic investigations

In situ Raman spectroscopy was applied to probe the interactions between adsorbed CO and Cu sites (Fig. S32). The Raman spectra were collected under potentiostatic conditions over the potential range from the open circuit potential (OCP) to − 0.58 V. At − 0.42 V, Cu NPs

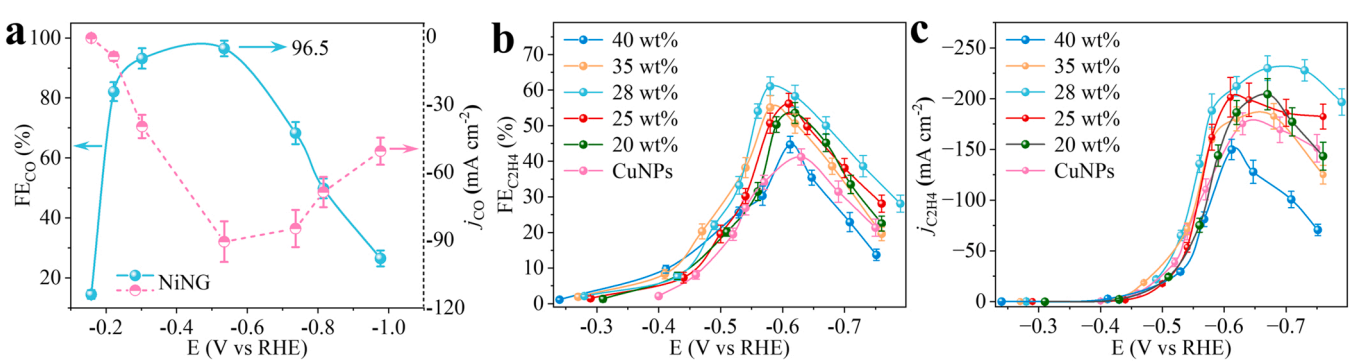

Fig. 5. ECO_2RR performances of catalysts on HG28 BCE GDLs. a, FE_{CO} and j_{CO} with NiNG. b,c, FE_{C2H4} (b) and j_{C2H4} (c) obtained with the CuNPs/NiNG tandem catalysts and CuNPs as a function of the applied potential. The weight percentage of NiNG in all CuNPs/NiNG tandem catalysts ranges from 20 to 40 wt%.

initially generated the Raman band at 1880–2130 cm^{-1} corresponding to the C≡O stretch associated with the adsorbed *atop*-bound CO (CO_{atop}) and *bridge*-bound CO (CO_{bridge}) [13,47–49]. In contrast, this band emerged at a more positive potential of − 0.36 V with CuNPs/28 wt% NiNG. This confirms that a CO enriched environment induced by NiNG facilitates C-C coupling and thus the generation of C_2H_4, as demonstrated by the ECO_2RR performance described above (Fig. 5b). Li et al. found that the ratio of CO_{atop} to CO_{bridge} (CO_{atop}/CO_{bridge}) played a critical role in controlling C_2H_4 formation during ECO_2RR [13]. To quantify the relationship between surface adsorbed CO and improved C_2H_4 productivity, the C≡O stretch band was deconvoluted using Lorentzian fitting (Fig. S33 and Fig. S34) [13]. A volcano-shaped relationship between FE_{C2H4} (or CO_{atop}/CO_{bridge} ratio) and NiNG wt% was found (Fig. 6a). This finding suggests that the CuNPs/28 wt% NiNG catalyst stabilizes more CO_{atop} on Cu sites than other CuNPs/NiNG tandem catalysts (Table S4). A higher loading of NiNG, although beneficial for CO formation, lowered the proportion of CO_{atop} because the number of active Cu sites decreased.

The effect of hydrophobicity-graded PTFE modification on the CO_2 reduction performance on 28 BCE coated with CuNPs/28 wt% NiNG or CuNPs also was probed quantitatively using Raman spectroscopy (Fig. 6b; Fig. 7a; Fig. S34). Lorentzian fitting of the bands showed that the hydrophobicity graded modification led to a ~0.06 increase in the CO_{atop}/CO_{bridge} ratio for both CuNPs and CuNPs/28 wt% NiNG catalysts (Fig. 6b, upper). This result implies that the hydrophobicity-graded treatment has the capability of tuning the micro-environment, i.e., the coverage of CO_{atop} and CO_{bridge} in the HG28 BCE based GDE during CO_2 electrolysis. Consequently, the FE_{C2H4} obtained with a HG28 BCE based GDE increased by ~5% in comparison with the unmodified one (Fig. 6b, bottom). This accounts for the superior j_{C2H4} values found with HG28 BCE based electrodes compared with those with 28 BCE based counterparts (Fig. 6c). In Fig. 7a, we compared the intensity of the Raman peaks obtained from the same catalyst coated on HG28 BCE and 28 BCE under the same experimental conditions. Compared to the 28 BCE based GDEs, the intensities associated with the Cu–CO bands were stronger on the HG28 BCE based GDEs while those associated with the adsorbed carbonates were suppressed (Fig. 7a). This finding also signified a higher adsorbed CO coverage and less carbonate production with the HG28 BCE based GDEs. The higher local CO concentration presumably arises from a higher local pressure across the HGGDL during electrolysis. Less carbonate formation mitigates the risk of salt precipitation, stabilizes the three-phase interface and facilitates interaction between CO_2 and catalysts, thereby stabilizing the CO_2-to-C_{2+} conversion (Fig. 7b).

To further evaluate the effect of HG28 BCE on the long-term stability of CO_2-to-C_2H_4 electrosynthesis, a cathode consisting of CuNPs/28 wt% NiNG tandem catalysts, and the HG28 BCE or raw 28 BCE was integrated into a membrane electrode assembly (MEA) (Fig. 7b, c, Fig. S35 – Fig. S40 **Supplementary Note 5**). The MEA setup was continuously operated at a constant current density of 183 mA cm^{-2} for 62 h and provided a stable C_2H_4 FE of 51 ± 5% and an average full-cell voltage of 3.6 V, representing an energy efficiency of 17% and single-pass CO_2 utilization of 1.2% for C_2H_4 (Fig. 7b). Under similar conditions, the MEA setup only exhibited a stable FE_{C2H4} of > 50% for ~5 h and an average full-cell voltage of 3.7 V when the unmodified 28 BCE GDL was used (Fig. 7c). On this basis, it is concluded that the hydrophobicity-graded strategy developed in this study can improve the stability duration period of commercial GDLs against flooding by an order of magnitude. Accordingly, the HGGDL-based electrode showcases the possibility for enhancing the overall performance of electrochemical conversion of CO_2 to ethylene at a level that is competitive with a PTFE membrane-based electrode (Table S5).

Quasi-operando XAS with a home-made flow cell setup was used to monitor the chemical and electronic structure variations of both Cu and Ni sites during ECO_2RR. The Ni K-edge XANES spectra revealed that the atomic Ni sites of the CuNPs/28 wt% NiNG were slightly reduced under catalytic turnover conditions (Fig. 7d). This is consistent with the linear combination fitting results that values of average oxidation states of Ni sites were sustained at ~ 1.03 – 1.14 in the cathodic potential range from − 0.36 V to − 0.79 V (Fig. S28 and Table S3). Under the same conditions, the Ni K-edge EXAFS spectra confirmed the stabilization of Ni–N bond and that no Ni–Ni bond was found (Fig. 7e and Fig. S37). Cu K-edge XANES and EXAFS spectra revealed that Cu sites maintained their metallic state during ECO_2RR (Fig. S38). These results confirm the stability of CuNPs/28 wt% NiNG catalyst under the ECO_2RR conditions, ruling out that rapid failure of CuNPs/28 wt% NiNG/28 BCE electrode originates from catalyst decay. Examination of the CuNPs/28 wt% NiNG/HG28 BCE GDE after electrolysis revealed that hydrophobicity-grade environment in HGGDE mitigates electrolyte flooding and salt precipitates (Fig. S39, Fig. S40 **Supplementary Note 5**).

4. Conclusion

We describe a simple and readily scalable method for the treatment of a commercial hydrophobic carbon GDL to obtain a hydrophobicity graded GDL with a narrower pore size distribution for stabilizing CO_2 reduction electrolysis. The treatment involves a series of processes that include PTFE coating, solvent cleaning, blowing, and sintering. The feasibility of the method was demonstrated by the fabrication of 3 types of HGGDLs derived from a range of commercial hydrophobic GDLs. Compared with the PMPL free counterparts, the NiNG catalyst deposited HGGDLs consistently exhibited enhanced ECO_2RR durability over 12 h in an alkaline liquid flow cell system. The origin of the stability

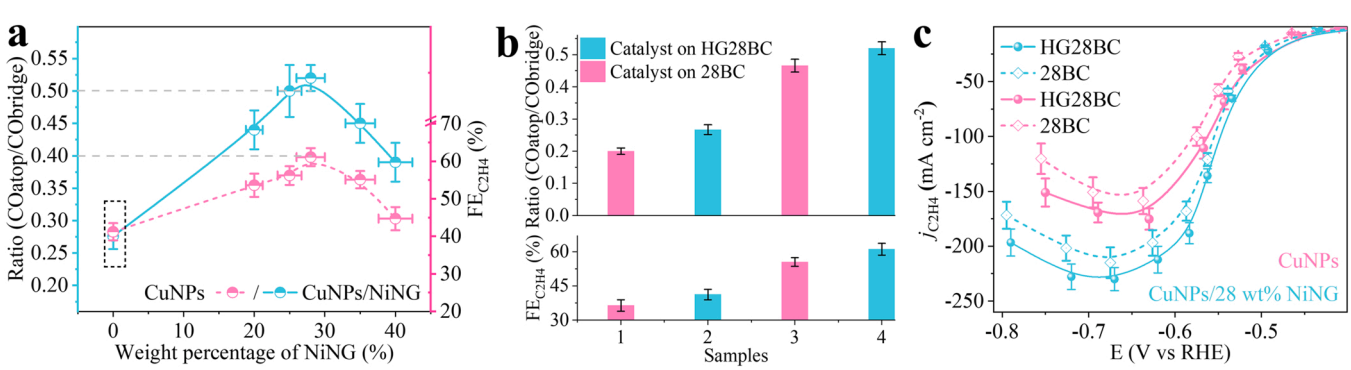

Fig. 6. CO adsorption mode in controlling the C_2H_4 production on HG28 BCE based GDEs. a, The correlation between the ratio of CO_{atop} and CO_{bridge} in CuNPs/NiNG catalysts, FE_{C2H4} and the weight percentage of NiNG in CuNPs/NiNG. b, The influence of HG28 BCE on the ratio of CO_{atop} to CO_{bridge} as well as FE_{C2H4}. Sample 1–2: CuNPs; 3–4: CuNPs/28 wt% NiNG. The ratios of CO_{atop} and CO_{bridge} were derived from Lorentzian fitting for the relevant bands in the *in situ* Raman spectra (Fig. S33, Fig. S34, Table S4). c, Comparison of j_{C2H4} with CuNPs/28 wt% NiNG (cyan) and CuNPs (pink) on GDLs as a function of the applied potential. The error bars in a-c represent one standard deviation based on three independent measurements.

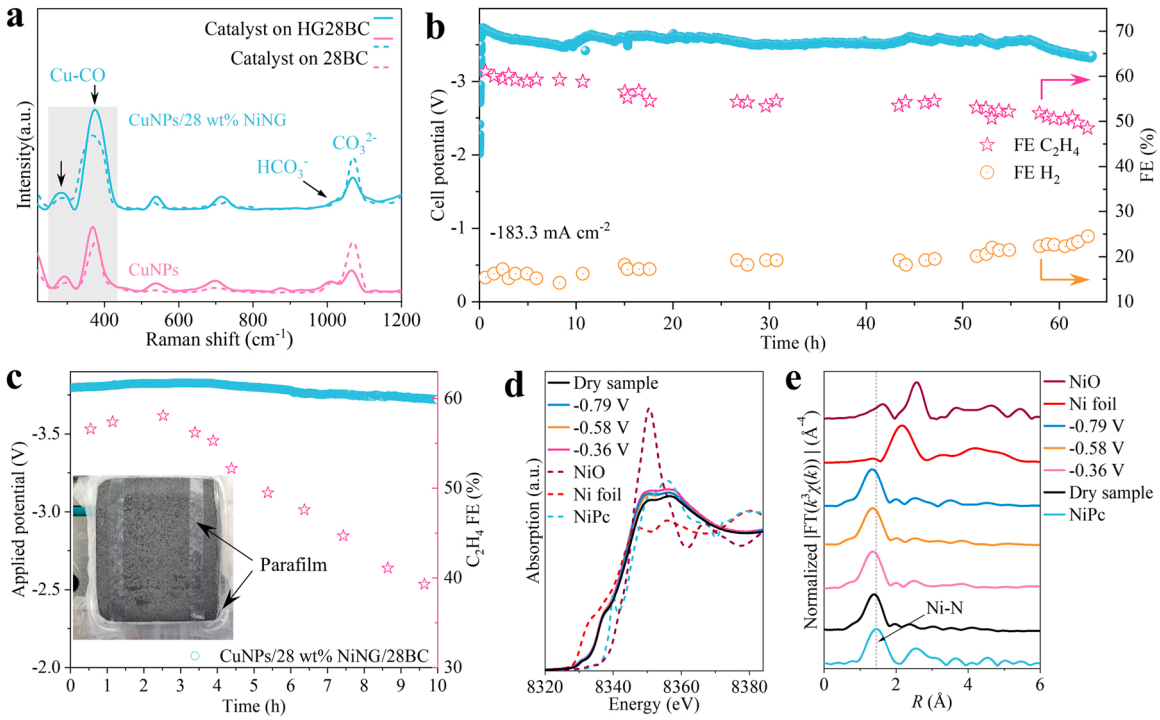

Fig. 7. Stability assessments with hydrophobicity graded electrodes. a, Raman spectra of CuNPs and CuNPs/28 wt% NiNG catalysts dispersed on 28 BCE (dashed lines) and HG28 BCE (solid lines), respectively. b,c, The stability was tested using a constant current of 183.3 mA cm^{-2} (without iR correction) with a MEA electrolyzer equipped with a cathode based on HG28 BCE (b) or 28 BCE GDL (c) and 0.15 M $KHCO_3$ anolyte. Inset in c: photograph of the free catalyst coated side of the cathode that has not been modified with PMPL. Detection of water drops dispersed on the cathode proves that the cathode became flooded during electrolysis. d,e, Quasi-operando Ni K-edge XANES and EXAFS spectra with the CuNPs/28 wt% NiNG catalyst as a function of applied potential.

enhancement was established by depositing CuNPs/NiNG tandem catalysts on HGGDLs. *In situ* Raman spectra data demonstrated that the tandem catalyst modified HGGDL could produce an inherently locally enriched CO environment adjacent to Cu sites, leading to enhanced ethylene selectivity relative to that found with the PMPL free counterparts. The higher local CO concentration reflects a higher local pressure across the HGGDL during electrolysis. The lower carbonate formation on HGGDL favours the stability of gas-solid-liquid three-phase interfaces in the HGGDL. With the hydrophobicity-graded procedure, we report an improved and stable production of ethylene (51 ± 5% FE) for 62 h using an HGGDL based GDE with a full-cell energy efficiency of 17% in neutral electrolyte medium, which is an order of magnitude higher than obtained with the unmodified GDE.

CRediT authorship contribution statement

J.Z. and A.M.B. supervised this project. L.L. carried out material synthesis, characterizations, electrochemical experiments and *in situ* Raman measurement. X.Z. contributed to revision. L. L. and Q.G. performed X-ray spectroscopy measurements and data analysis. J.C. and V. S.S.M. carried out AC-HAADF-STEM measurements. L. L., J.Z., A.M.B. and C. L. wrote the manuscript. All authors discussed the results and assisted with manuscript preparation.

Declaration of Competing Interest

The authors declare that they have no known competing financial interests or personal relationships that could have appeared to influence the work reported in this paper.

Data Availability

Data will be made available on request.

Acknowledgements

This research was supported by the Australian Research Council (ARC) through the ARC Centre of Excellence for Electromaterials Science (grant no. CE140100012). The authors acknowledge use of the facilities at Monash Centre for Electron Microscopy funded by the Australian Research Council (grant no. LE0454166) and and the access to Australian National Fabrication Facility (ANFF) - Materials Node at University of Wollongong (UOW). Assistance of Yvonne Hora from the Monash X-ray Platform also is greatly acknowledged.

Appendix A. Supporting information

Supplementary data associated with this article can be found in the online version at doi:10.1016/j.apcatb.2023.122597.

References

[1] W.R. Leow, Y. Lum, A. Ozden, Y. Wang, D.H. Nam, B. Chen, J. Wicks, T.T. Zhuang, F. Li, D. Sinton, E.H. Sargent, Chloride-mediated selective electrosynthesis of ethylene and propylene oxides at high current density, Science 368 (2020) 1228–1233.
[2] P. Zhu, H. Wang, High-purity and high-concentration liquid fuels through CO_2 electroreduction, Nat. Catal. 4 (2021) 943–951.
[3] Y. Hori, H. Wakebe, T. Tsukamoto, O. Koga, Electrocatalytic process of CO selectivity in electrochemical reduction of CO_2 at metal electrodes in aqueous media, Electrochim. Acta 39 (1994) 1833–1839.
[4] C. Xia, P. Zhu, Q. Jiang, Y. Pan, W. Liang, E. Stavitsk, H.N. Alshareef, H. Wang, Continuous production of pure liquid fuel solutions via electrocatalytic CO_2 reduction using solid-electrolyte devices, Nat. Energy 4 (2019) 776–785.
[5] J. Wu, T. Sharifi, Y. Gao, T. Zhang, P.M. Ajayan, Emerging carbon-based heterogeneous catalysts for electrochemical reduction of carbon dioxide into value-added chemicals, Adv. Mater. 31 (2019), 1804257.
[6] M. Jouny, W. Luc, F. Jiao, General techno-economic analysis of CO_2 electrolysis systems, Ind. Eng. Chem. Res. 57 (2018) 2165–2177.
[7] Y. Hori, I. Takahashi, O. Koga, N. Hoshi, Selective formation of C2 compounds from electrochemical reduction of CO_2 at a series of copper single crystal electrodes, J. Phys. Chem. B 106 (2002) 15–17.

[8] P. De Luna, R. Quintero-Bermudez, C.T. DInh, M.B. Ross, O.S. Bushuyev, P. Todorović, T. Regier, S.O. Kelley, P. Yang, E.H. Sargent, Catalyst electro-redeposition controls morphology and oxidation state for selective carbon dioxide reduction, Nat. Catal. 1 (2018) 103–110.

[9] Y. Wang, Z. Wang, C.T. Dinh, J. Li, A. Ozden, M. Golam Kibria, A. Seifitokaldani, C. S. Tan, C.M. Gabardo, M. Luo, H. Zhou, F. Li, Y. Lum, C. McCallum, Y. Xu, M. Liu, A. Proppe, A. Johnston, P. Todorovic, T.T. Zhuang, D. Sinton, S.O. Kelley, E. H. Sargent, Catalyst synthesis under CO_2 electroreduction favours faceting and promotes renewable fuels electrosynthesis, Nat. Catal. 3 (2020) 98–106.

[10] T.T.H. Hoang, S. Verma, S. Ma, T.T. Fister, J. Timoshenko, A.I. Frenkel, P.J. A. Kenis, A.A. Gewirth, Nanoporous copper-silver alloys by additive-controlled electrodeposition for the selective electroreduction of CO_2 to ethylene and ethanol, J. Am. Chem. Soc. 140 (2018) 5791–5797.

[11] E.L. Clark, C. Hahn, T.F. Jaramillo, A.T. Bell, Electrochemical CO_2 reduction over compressively strained CuAg surface alloys with enhanced multi-carbon oxygenate selectivity, J. Am. Chem. Soc. 139 (2017) 15848–15857.

[12] D.H. Nam, O.S. Bushuyev, J. Li, P. De Luna, A. Seifitokaldani, C.T. Dinh, F.P. García De Arquer, Y. Wang, Z. Liang, A.H. Proppe, C.S. Tan, P. Todorović, O. Shekhah, C. M. Gabardo, J.W. Jo, J. Choi, M.J. Choi, S.W. Baek, J. Kim, D. Sinton, S.O. Kelley, M. Eddaoudi, E.H. Sargent, Metal-organic frameworks mediate Cu coordination for selective CO_2 electroreduction, J. Am. Chem. Soc. 140 (2018) 11378–11386.

[13] F. Li, A. Thevenon, A. Rosas-Hernández, Z. Wang, Y. Li, C.M. Gabardo, A. Ozden, C. T. Dinh, J. Li, Y. Wang, J.P. Edwards, Y. Xu, C. McCallum, L. Tao, Z.Q. Liang, M. Luo, X. Wang, H. Li, C.P. O'Brien, C.S. Tan, D.H. Nam, R. Quintero-Bermudez, T. T. Zhuang, Y.C. Li, Z. Han, R.D. Britt, D. Sinton, T. Agapie, J.C. Peters, E. H. Sargent, Molecular tuning of CO_2-to-ethylene conversion, Nature 577 (2020) 509–513.

[14] X. Chen, J. Chen, N.M. Alghoraibi, D.A. Henckel, R. Zhang, U.O. Nwabara, K. E. Madsen, P.J.A. Kenis, S.C. Zimmerman, A.A. Gewirth, Electrochemical CO_2-to-ethylene conversion on polyamine-incorporated Cu electrodes, Nat. Catal. 4 (2021) 20–27.

[15] D.M. Weekes, D.A. Salvatore, A. Reyes, A. Huang, C.P. Berlinguette, Electrolytic CO_2 reduction in a flow cell, Acc. Chem. Res. 51 (2018) 910–918.

[16] D. Wakerley, S. Lamaison, J. Wicks, A. Clemens, J. Feaster, D. Corral, S.A. Jaffer, A. Sarkar, M. Fontecave, E.B. Duoss, S. Baker, E.H. Sargent, T.F. Jaramillo, C. Hahn, Gas diffusion electrodes, reactor designs and key metrics of low-temperature CO_2 electrolysers, Nat. Energy 7 (2022) 130–143.

[17] L. Cindrella, A.M. Kannan, J.F. Lin, K. Saminathan, Y. Ho, C.W. Lin, J. Wertz, Gas diffusion layer for proton exchange membrane fuel cells-a review, J. Power Sources 194 (2009) 146–160.

[18] J. Zhou, S. Shukla, A. Putz, M. Secanell, Analysis of the role of the microporous layer in improving polymer electrolyte fuel cell performance, Electrochim. Acta 268 (2018) 366–382.

[19] Y. Kong, M. Liu, H. Hu, Y. Hou, S. Vesztergom, M. de, J. Gálvez-Vázquez, I. Zelocualtecatl Montiel, V. Kolivoška, P. Broekmann, Cracks as efficient tools to mitigate flooding in gas diffusion electrodes used for the electrochemical reduction of carbon dioxide, Small Methods 6 (2022), 2200369.

[20] M.E. Leonard, L.E. Clarke, A. Forner-Cuenca, S.M. Brown, F.R. Brushett, Investigating electrode flooding in a flowing electrolyte, gas-fed carbon dioxide electrolyzer, ChemSusChem 13 (2020) 400–411.

[21] K. Yang, R. Kas, W.A. Smith, T. Burdyny, Role of the carbon-based gas diffusion layer on flooding in a gas diffusion electrode cell for electrochemical CO_2 reduction, ACS Energy Lett. 6 (2021) 33–40.

[22] L. Li, J. Chen, V.S.S. Mosali, Y. Liang, A.M. Bond, Q. Gu, J. Zhang, Hydrophobicity graded gas diffusion layer for stable electrochemical reduction of CO_2, Angew. Chem. Int. Ed. 61 (2022), e202208534.

[23] C. Chen, Y. Li, P. Yang, Address the "alkalinity problem" in CO_2 electrolysis with catalyst design and translation, Joule 5 (2021) 737–742.

[24] M. Luo, Z. Wang, Y.C. Li, J. Li, F. Li, Y. Lum, D.H. Nam, B. Chen, J. Wicks, A. Xu, T. Zhuang, W.R. Leow, X. Wang, C.T. Dinh, Y. Wang, Y. Wang, D. Sinton, E. H. Sargent, Hydroxide promotes carbon dioxide electroreduction to ethanol on copper via tuning of adsorbed hydrogen, Nat. Commun. 10 (2019) 5814.

[25] K. Yang, R. Kas, W.A. Smith, In Situ infrared spectroscopy reveals persistent alkalinity near electrode surfaces during CO_2 electroreduction, J. Am. Chem. Soc. 141 (2019) 15891–15900.

[26] A. El-kharouf, B.G. Pollet, Gas Diffusion Media and Their Degradation, Elsevier Inc, 2012.

[27] K. Liu, W.A. Smith, T. Burdyny, Introductory guide to assembling and operating gas diffusion electrodes for electrochemical CO_2 reduction, ACS Energy Lett. 4 (2019) 639–643.

[28] Y. Wu, L. Charlesworth, I. Maglaya, M.N. Idros, M. Li, T. Burdyny, G. Wang, T. E. Rufford, Mitigating electrolyte flooding for electrochemical CO_2 reduction via infiltration of hydrophobic particles in a gas diffusion layer, ACS Energy Lett. 7 (2022) 2884–2892.

[29] X. Wang, J.F. de Araújo, W. Ju, A. Bagger, H. Schmies, S. Kühl, J. Rossmeisl, P. Strasser, Mechanistic reaction pathways of enhanced ethylene yields during electroreduction of CO_2–CO co-feeds on Cu and Cu-tandem electrocatalysts, Nat. Nanotechnol. 14 (2019) 1063–1070.

[30] S. Nitopi, E. Bertheussen, S.B. Scott, X. Liu, A.K. Engstfeld, S. Horch, B. Seger, I.E. L. Stephens, K. Chan, C. Hahn, J.K. Nørskov, T.F. Jaramillo, I. Chorkendorff, Progress and perspectives of electrochemical CO_2 reduction on copper in aqueous electrolyte, Chem. Rev. 119 (2019) 7610–7672.

[31] C. Xiao, J. Zhang, Architectural design for enhanced c2 product selectivity in electrochemical CO_2 reduction using Cu-based catalysts: a review, ACS Nano 15 (2021) 7975–8000.

[32] D.L. Meng, M. Di Zhang, D.H. Si, M.J. Mao, Y. Hou, Y.B. Huang, R. Cao, Highly selective tandem electroreduction of CO_2 to ethylene over atomically isolated nickel–nitrogen site/copper nanoparticle catalysts, Angew. Chem. - Int. Ed. 60 (2021) 25485–25492.

[33] Y. Lee, J. Choi, K.J. Lee, N.E. Stott, D. Kim, Large-scale synthesis of copper nanoparticles by chemically controlled reduction for applications of inkjet-printed electronics, Nanotechnology 19 (2008), 415604.

[34] W. Luc, J. Rosen, F. Jiao, An Ir-based anode for a practical CO_2 electrolyzer, Catal. Today 288 (2017) 79–84.

[35] J.E. Huang, F. Li, A. Ozden, A.S. Rasouli, F.P.G. de Arquer, S. Liu, S. Zhang, M. Luo, X. Wang, Y. Lum, Y. Xu, K. Bertens, R.K. Miao, C.T. Dinh, D. Sinton, E.H. Sargent, CO_2 electrolysis to multicarbon products in strong acid, Science 372 (2021) 1074–1078.

[36] C.M. Simon, W. Kaminsky, Chemical recycling of polytetrafluoroethylene by pyrolysis, Polym. Degrad. Stab. 62 (1998) 1–7.

[37] O.J. Whittemore, J.A. Varela, Pore growth and shrinkage during sintering, Sinter. Key Pap. (1990) 777–792.

[38] M.A. Pouchon, L.A. Nordström, C. Hellwig. Modeling of sphere-pac fuel, 1st ed., Elsevier Inc, 2012.

[39] I. Cristofolini, A. Rao, C. Menapace, A. Molinari, Influence of sintering temperature on the shrinkage and geometrical characteristics of steel parts produced by powder metallurgy, J. Mater. Process. Technol. 210 (2010) 1716–1725.

[40] Encyclopedia of physical science and technology, Choice Rev. Online. (2002).

[41] R.J.M. Konings, T. Allen, R. Stoller, S. Yamanaka, Comprehensive nuclear materials, 2012.

[42] Z. Xing, L. Hu, D.S. Ripatti, X. Hu, X. Feng, Enhancing carbon dioxide gas-diffusion electrolysis by creating a hydrophobic catalyst microenvironment, Nat. Commun. 12 (2021) 136.

[43] B. De Mot, J. Hereijgers, M. Duarte, T. Breugelmans, Influence of flow and pressure distribution inside a gas diffusion electrode on the performance of a flow-by CO_2 electrolyzer, Chem. Eng. J. 378 (2019), 122224.

[44] F. Li, Y.C. Li, Z. Wang, J. Li, D.H. Nam, Y. Lum, M. Luo, X. Wang, A. Ozden, S. F. Hung, B. Chen, Y. Wang, J. Wicks, Y. Xu, Y. Li, C.M. Gabardo, C.T. Dinh, Y. Wang, T.T. Zhuang, D. Sinton, E.H. Sargent, Cooperative CO_2-to-ethanol conversion via enriched intermediates at molecule–metal catalyst interfaces, Nat. Catal. 3 (2020) 75–82.

[45] D.H. Nam, P. De Luna, A. Rosas-Hernández, A. Thevenon, F. Li, T. Agapie, J. C. Peters, O. Shekhah, M. Eddaoudi, E.H. Sargent, Molecular enhancement of heterogeneous CO_2 reduction, Nat. Mater. 19 (2020) 266–276.

[46] W. Ma, S. Xie, T. Liu, Q. Fan, J. Ye, F. Sun, Z. Jiang, Q. Zhang, J. Cheng, Y. Wang, Electrocatalytic reduction of CO_2 to ethylene and ethanol through hydrogen-assisted C–C coupling over fluorine-modified copper, Nat. Catal. 3 (2020) 478–487.

[47] Y.C. Li, Z. Wang, T. Yuan, D.H. Nam, M. Luo, J. Wicks, B. Chen, J. Li, F. Li, F.P. G. De Arquer, Y. Wang, C.T. Dinh, O. Voznyy, D. Sinton, E.H. Sargent, Binding site diversity promotes CO_2 electroreduction to ethanol, J. Am. Chem. Soc. 141 (2019) 8584–8591.

[48] J. Heyes, M. Dunwell, B. Xu, CO_2 reduction on Cu at low overpotentials with surface-enhanced in situ spectroscopy, J. Phys. Chem. C. 120 (2016) 17334–17341.

[49] W. Akemann, A. Otto, Vibrational modes of CO adsorbed on disordered copper films, J. Raman Spectrosc. 22 (1991) 797–803.